AGU PUBLICATIONS

JGR

Journal of Geophysical Research: Solid Earth

RESEARCH ARTICLE
10.1002/2014JB011353

Key Points:
- A midcrustal LVZ is observed in the Precambrian Canadian Shield
- LVZ is 10+ km thick and over 200 km wide with granitic composition
- LVZ is caused by the crust melting during the Precambrian orogenesis

Supporting Information:
- Figures S1 and S2

Correspondence to:
Y. J. Gu,
ygu@ualberta.ca

Citation:
Chen, Y., Y. J. Gu, R. M. H. Dokht, and M. D. Sacchi (2015), Crustal imprints of Precambrian orogenesis in western Laurentia, *J. Geophys. Res. Solid Earth*, *120*, 6993–7012, doi:10.1002/2014JB011353.

Received 5 JUN 2014
Accepted 19 AUG 2015
Accepted article online 25 AUG 2015
Published online 12 OCT 2015

Crustal imprints of Precambrian orogenesis in western Laurentia

Yunfeng Chen[1], Yu Jeffrey Gu[1], Ramin M. H. Dokht[1], and Mauricio D. Sacchi[1]

[1]Department of Physics, University of Alberta, Edmonton, Alberta, Canada

Abstract Crustal low-velocity zones (LVZs) have been reported in active orogens such as the Himalayas and the Andes but rarely in stable cratonic regions. In this study, we provide compelling evidence for a significant midcrustal LVZ beneath eastern-central Alberta, an integral part of the Precambrian Canadian Shield covered by thick Phanerozoic sedimentary deposits. This 200 km wide, over 10 km thick midcrustal LVZ is well resolved by shear velocity inversions using P-to-S receiver functions from more than 4600 earthquakes. It is generally overlain by a high-velocity upper crust in the depth range of 8–15 km, especially in western-central Alberta, which coincides with the previously documented Winagami reflection sequence. We interpret the LVZ to be of granitic composition, potentially in connection with the crystallization of partially molten crust during the Paleoproterozoic eon. In addition to the Precambrian tectonic history of western Laurentia, which featured plate convergence conducive to crustal melting, our crustal model is further supported by (1) a moderate spatial correlation between the LVZ and heat flow, and (2) shear velocities consistent with that of granite. The well preserved Winagami reflection sequence and the LVZ are potential evidence of distinct episodes of magmatism and crust modification in the Precambrian basement of the Western Canada Sedimentary Basin. The existence of a broad crustal LVZ suggests extensive subduction, orogenesis, and crustal melting during the Precambrian assembly of the North American craton.

1. Introduction

Crustal low-velocity zones (LVZs) have been widely reported based on geophysical observations from various disciplines, most notably wide-angle seismic reflection and refraction [*Nelson et al.*, 1996; *Masson et al.*, 1998], ambient noise tomography [*Li et al.*, 2010; *Yang et al.*, 2012], magnetotellurics [*Wei et al.*, 2001; *Unsworth et al.*, 2005], and earthquakes from teleseismic distances [*Kind et al.*, 1995; *Beck and Zandt*, 2002]. Their formation has been attributed to a number of plausible mechanisms depending on the genesis and evolution of the resident tectonic province [*Li et al.*, 2003a, 2003b; *Yang et al.*, 2012; *Ward et al.*, 2013]. In active orogens such as the central Andes and the Tibetan Plateau [*Nelson et al.*, 1996], crustal LVZs could signify the presence of magma bodies [*Chmielowski et al.*, 1999] or zones of partial melting in thickened crust [*Kind et al.*, 1996; *Yuan et al.*, 1997]. Fluid-filled cracks [*Stern et al.*, 2007] and aquifer layers [*Li et al.*, 2003a; *Yang et al.*, 2012] due to metamorphic dehydration, or extensive serpentine channels atop slabs [*Abers*, 2005] are also capable of severely reducing crustal seismic velocities. Under favorable pressure and temperature conditions, magmatic and metamorphic processes often alter the composition of the protolith and induce low-velocity, felsic granite intrusions into middle and/or upper crustal depths [*Petford et al.*, 2000]. Some of these granite bodies have been identified through surface exposures, as in the case of Aletschhorn Mountain, New Zealand [*Mueller*, 1977], while the majority are embedded in basement rocks resembling those beneath Variscan, southwestern Ireland [*Masson et al.*, 1998] and Guangdong, southeastern China [*Chen and Grapes*, 2007].

Crustal LVZs are generally the byproduct of collisional tectonics, manifested either by the subduction of oceanic crust [*Yuan et al.*, 2000] or by continent-continent convergence that forms impressive mountain ranges. A contemporary example of the latter scenario is the Himalaya-Karakoram-Tibetan Orogen [*St-Onge et al.*, 2006], where LVZs at midcrustal depths effectively delineate the Cenozoic suture zone between the Indian and Eurasian plates. LVZs can also provide forensic evidence for the formation of the Precambrian crust during tectonomagmatic episodes [*James et al.*, 2003]. One prime example is the Trans-Hudson Orogen (THO) in North America. As one of the largest orogens in the early Proterozoic, the THO extends more than 1000 km from the western Superior province to the Snowbird Tectonic Zone (STZ) [*Ross et al.*, 1995] and approximately 3000 km

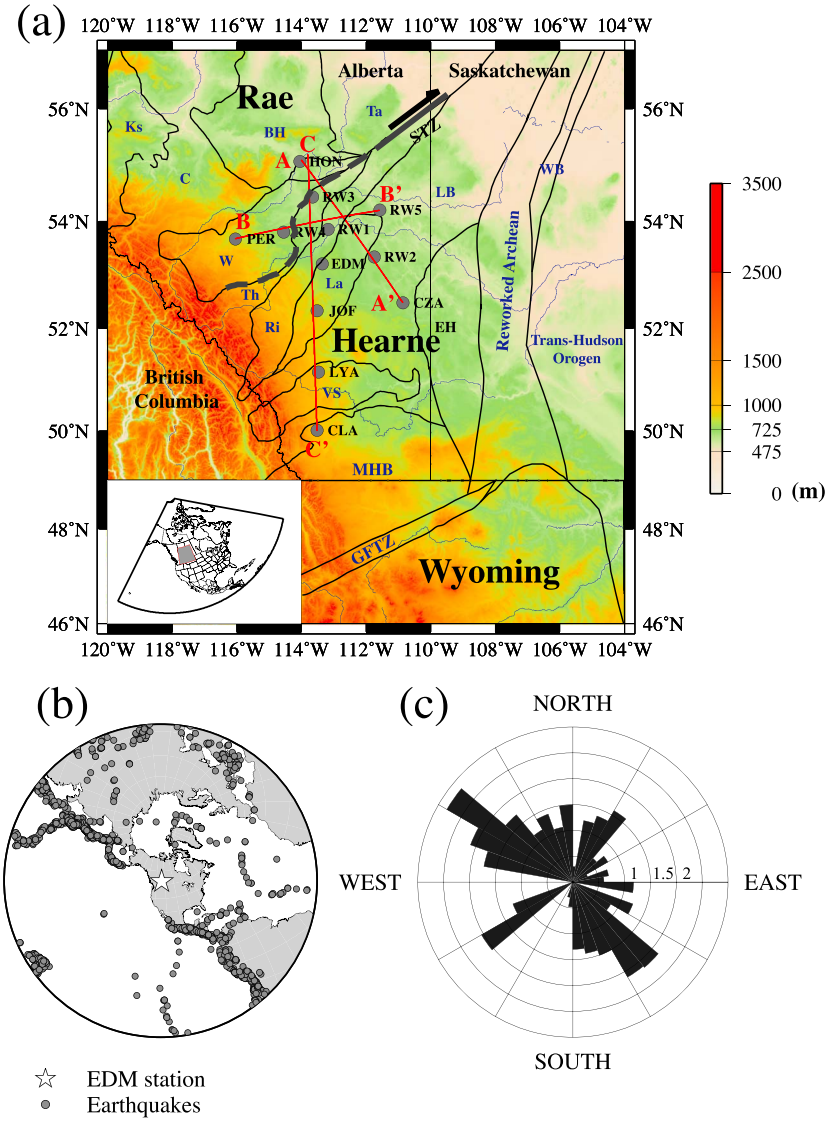

Figure 1. (a) Broadband seismic stations superimposed on a regional topographic map. A-A', B-B', and C-C' are three cross sections for detailed comparisons of velocity variations across the array (see Figure 5). The thick dashed line marks the speculated location of the subsurface extension of the STZ beneath the WCSB. LB, Loverna block; La, Lacombe domain; Ri, Rimbey domain; Th, Thorsby domain; W, Wabamun domain; MHB, Medicine Hat block; VS, Vulcan structure; BH, Buffalo Head; Ta, Taltson; C, Chinchaga; Ks, Ksituan; STZ, Snowbird Tectonic Zone; GFTZ, Great Falls Tectonic Zone. (b) Epicenter locations for all events used in this study. The star marks the location of station EDM. (c) A rose diagram showing the distribution of data azimuths on a logarithmic scale.

along strike from South Dakota to the Ungava Peninsula in northern Quebec [*Corrigan et al.*, 2009]. With comparable scale, duration, and characteristics to the Cenozoic Himalayas, the THO potentially marks the collisional suture that welded several Precambrian plates together during the assembly of the North American craton [*Hoffman*, 1988]. Extensive crustal shortening and thickening, as well as tectonothermal activities of metamorphism and magmatism [*St-Onge et al.*, 2006], may have transpired around the THO in a similar fashion to more recent events surrounding the Tibetan Plateau. However, a Himalayan-scale LVZ has not been documented within the Precambrian crust in the vicinity of the Paleoproterozoic THO.

This paper introduces new seismological constraints on the crustal structure beneath central Alberta, a region strongly influenced by the tectonic events surrounding the THO. The region of study (Figure 1a) is a complex

assembly largely consisted of the southern Hearne and Rae provinces [*Ross et al.*, 1991]. Bounded by the THO (east) and the STZ (west), a possible suture zone along the Rae province [*Berman et al.*, 2007], the Archean Hearne craton is generally regarded as a reworked hinterland [*Lucas et al.*, 1993] that stretches northeasterly from the foothills of the Rockies to the Hudson Bay. A large-scale batholith (Wathaman-Chipewyan batholith) has been discovered in the northeastern Hearne province [*Lewry et al.*, 1981] and attributed to the emplacement of crystallized, felsic plutonic rocks in connection with the Proterozoic collision between the Hearne craton and the accreted terranes [*Corrigan et al.*, 2009]. Proterozoic magmatism has also been documented in the southern Rae province [*Ross and Eaton*, 1997; *Welford and Clowes*, 2006], but the tectonic evolution of southwestern STZ and the Hearne, the focus of this study (Figure 1a), remains debated due to the thick Phanerozoic cover in the Western Canada Sedimentary Basin (WCSB) [*Shragge et al.*, 2002].

2. Geophysical Investigations in the Study Region

The understanding of the basement assembly and evolution in southwestern Laurentia greatly benefited from regional seismic surveys such as deep-sounding reflection experiments (e.g., Central Alberta Transect [*Clowes et al.*, 1996] and Southern Alberta Lithospheric Transect [*Eaton et al.*, 1999]), teleseisms [*Eaton and Cassidy*, 1996; *Shragge et al.*, 2002], and controlled source refraction experiments [*Clowes et al.*, 2002]. The successes of these surveys are unquestioned, which marked a milestone in the integrated effort to map the regional crust and upper mantle structures beneath western Canada. On the other hand, the linear receiver geometries of the reflection/refraction surveys and the sparse distribution of broadband seismic sensors represented major limitations in data coverage within the WCSB [*Gu et al.*, 2011]. Consequently, southern WCSB was undersampled and critical issues such as the origin of the STZ and the integrity of the mantle lithosphere remain debated [*Ross et al.*, 2000; *Shragge et al.*, 2002; *Flowers et al.*, 2006; *Berman et al.*, 2007].

The establishment of the Canadian Rockies and Alberta Network (CRANE) [*Gu et al.*, 2011], which began in mid-2006, spearheaded the development of regional seismic monitoring [*Gu et al.*, 2009; *Stern et al.*, 2013] and analysis [*Gu*, 2010; *Gu and Shen*, 2012; *Schultz et al.*, 2014; *Gu and Shen*, 2015; *Gu et al.*, 2015] in Alberta. With an average station spacing of ~250 km, CRANE provides semi-uniform broadband data coverage necessary for a preliminary 3-D survey of its underlying crust and mantle in central Alberta [*Gu et al.*, 2011; *Gu and Shen*, 2015; *Gu et al.*, 2015]. In this study, we combine teleseismic data from CRANE and a Canadian National Seismic Network (CNSN) station to improve the constraints on the crustal structure of southern WCSB. Our new findings offer compelling evidence for a midcrustal LVZ, which we interpret as a previously undisclosed granitic body formed by syn-collisional and/or post-collisional magmatic activities during the Proterozoic eon. This orogenic imprint lends new insights into the Proterozoic tectonic evolution of the North American craton.

3. Data and Method

Our data set consists of continuous waveforms from EDM, a permanent broadband seismic station from CNSN, and 11 CRANE stations in central and southern Alberta (Figure 1a). Since the deployment of the first station in 2006, CRANE has recorded 1500 $M_w > 5.5$ earthquakes in the epicentral distance range of 30 to 90°, which are ideal for a RF analysis where teleseismic *P* waves produce observable *S* conversions at crust and mantle interfaces [*Burdick and Langston*, 1977; *Owens et al.*, 1984; *Cassidy*, 1992].

Our data processing scheme is similar to that of *Crotwell and Owens* [2005]. After isolating the *P* wave coda using a time window of 150 s, we rotate the three-component data to the great circle coordinate system and apply a Butterworth bandpass filter with corner frequencies of 0.3 and 5.0 Hz. The signal-to-noise ratio (SNR), which is defined by the ratio between the variances of the signal (1 s before and 5 s after predicted *P* arrival time) and noise (105 to 5 s prior to *P*) windows, is used as a criterion for quality control; 1891 seismograms with SNR > 2 were retained for further RF processing. To estimate the RFs, we deconvolve the vertical component from the radial component seismograms using the water-level deconvolution method [*Clayton and Wiggins*, 1976; *Owens et al.*, 1984; *Mangino et al.*, 1993]. High-frequency noise embedded in the RFs is subsequently minimized through a Gaussian filter where the filter width parameter controls the frequency content. To resolve structures at different wavelengths and to ensure self-consistency, we subject each RF to Gaussian filters with corners at 0.6 and 2.4 Hz, which correspond to filter width parameters of 1.25 and 5, respectively. The last step of preprocessing is manual quality control where all RFs are visually

Table 1. Number of Traces Retained After Each Processing Step[a]

Station	Number of Seismograms	Number of Seismograms With SNR > 2	Number of RFs with 80% Energy (Low/High)	Number of Manually Selected RFs (Low/High)
RW1	214	54	33/39	10/12
RW2	214	65	46/44	19/20
RW3	211	59	32/30	8/14
RW4	192	47	26/30	7/10
RW5	205	9	6/6	2/2
JOF	75	46	32/32	8/8
CZA	450	243	165/167	64/66
PER	575	322	218/237	68/88
HON	291	79	57/63	17/22
CLA	465	98	38/49	6/5
LYA	262	131	83/91	16/19
EDM	1512	738	560/552	169/221
Total	4666	1891	692/691	396/487

[a]This table shows the remaining number of traces for every processing step at each station. The fourth column shows the number of RFs that recover 80% energy on the radial component seismograms. The total number of traces for the entire array is listed in the last row.

inspected; RFs exhibiting high presignal noise or abnormally strong reverberations are eliminated. We retain 396 and 487 traces for the low- and high-frequency RFs, respectively (Table 1).

The resulting high-quality RFs are subsequently corrected for epicentral distance, a vital procedure for the proper alignments of key phases such as the Moho conversion (Pms) and the subsequent reverberations (PpPms and PsPms + PpSms). The move-out effects of these phases are minimized by stretching or contracting the RFs with respect to a reference trace of 60° distance following the "four-pin" method [*Chen and Niu*, 2013]; this approach ensures the proper rescaling of RFs based on ray parameters. The amplitude of the time-corrected RF is subsequently modified by the ray parameter ratio between the reference RF and the RF in question [*Chen and Niu*, 2013]. After the time and amplitude corrections, we stack the aligned RFs to produce a single RF estimate for each station and retrieve the shear velocity structure based on the iterative linear inversion approach of *Ammon et al.* [1990]. We adopt a starting crustal/upper mantle structure that combines different regional models [*Zelt and Ellis*, 1989; *Eaton and Cassidy*, 1996; *Bouzidi et al.*, 2002; *Shragge et al.*, 2002]. The upper 80 km of the starting model consists of a sedimentary layer (0–3 km) [*Eaton and Cassidy*, 1996] and a crystalline basement (4–80 km) modified after *Bouzidi et al.* [2002]. The underlying lithosphere down to 200 km depth is represented by AK135 [*Kennett et al.*, 1995]. We further modify the Moho depth and Poisson's ratio in the starting model based on the H-K results of *Contenti et al.* [2012], which properly considers the timing of the Moho conversion and reverberations in the synthetic RFs during inversion. It is worth noting that, despite our best efforts to construct a reasonable starting model, results of linear inversions of RFs are inevitably affected by the nonuniqueness of the solutions [*Ammon et al.*, 1990]. Hence, we perform a sequence of 16 inversions for each station with starting models obtained by adding 0.5 km/s cubic velocity perturbations [*Ammon et al.*, 1990] and up to 0.1 km/s random velocity perturbations [see *Ammon et al.*, 1990] to the initial model. The resulting models are selected based on the reduction of data variance as well as the velocity characteristics: models with 25% or greater residual (i.e., data - prediction) energy are subsequently removed. This selection criterion results in 10–16 candidate models, which are subsequently averaged to produce the optimal starting model for the final inversion for each station.

4. Results

4.1. Preliminary Assessments

The stacked RFs, especially the low-frequency RFs, exhibit similar waveforms (Figure 2) across the array. Moho conversions (Pms) are clearly identified at ~5 s, e.g., 4.9 s for station EDM, after the *P* wave signal. For the Moho depth calculation beneath station EDM, we adopt a *Vp*/*Vs* ratio of 1.776 based on the result of a recent H-K analysis [*Contenti et al.*, 2012] and an average crustal *P* velocity of 6.3 km/s estimated from CRUST 1.0 [*Laske et al.*, 2013]. The timing of the Moho conversions translates to a depth of 38.5 km, which is in excellent agreement with the regional average reported by *Bouzidi et al.* [2002] (40.0 km) from seismic reflection data

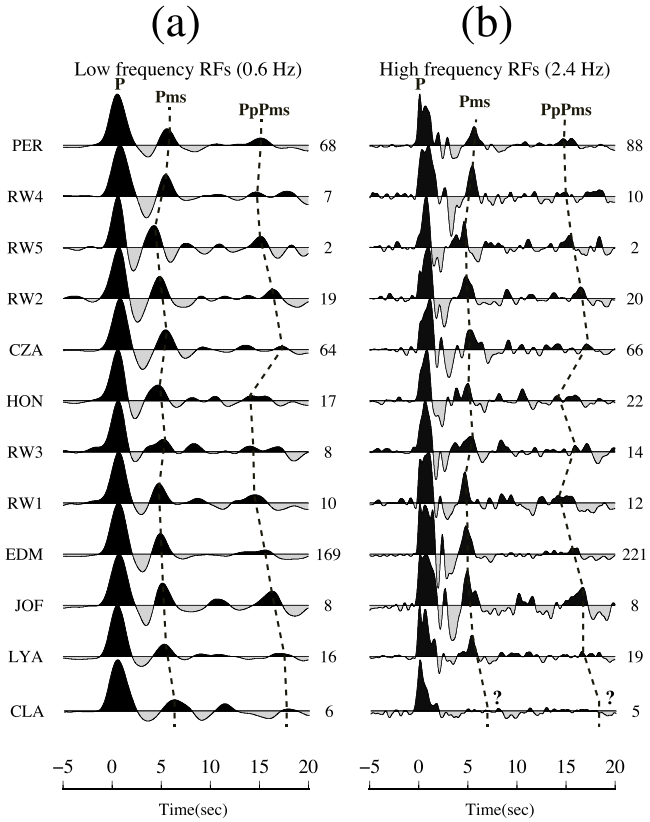

Figure 2. Waveforms of stacked RFs at (a) low (0.6 Hz) and (b) high (2.4 Hz) frequencies. The numbers beside the RFs shows the numbers of traces from the respective stations. The dotted lines mark the peaks of the direct (*P*), Moho converted (Pms), and reverberated (PpPms) phases.

and *Shragge et al.* [2002] (38.5 km) from teleseismic RFs. In addition to Moho conversions, the vast majority of the low frequency RFs show a negative phase at 3–4 s, which often suggests zones of velocity reversal above the Moho [*Kumar et al.*, 2002; *Monsalve et al.*, 2013]. In comparison, the high-frequency RFs show more complex waveforms, though similar negative amplitudes can be identified on a number of RFs. It is worth noting that the direct *P* waves at higher frequencies are generally offset from zero due to the existence of conversions and reverberations within the sedimentary basin [*Cassidy*, 1992; *Sheehan et al.*, 1995]. With the exception of station CLA, the Moho conversions (Pms) on all RFs are visible in the time range of 5–6 s.

4.2. High-Velocity Upper Crust

One of the persistent features of the inverted models in the WCSB is a high-velocity upper crust. Rather than a gradational structure in simplified regional models [*Kanasewich et al.*, 1969; *Bouzidi et al.*, 2002], the majority of the model speeds exceed 3.55 km/s between 5 and 12 km depths and show a negative gradient at 12–15 km. This high-velocity zone (HVZ) is especially prominent beneath western stations (e.g., RW4 and PER) from CRANE, showing average velocities as high as 3.87 km/s. The existence of an upper crustal HVZ has been documented previously and attributed to the Winagami reflection sequence (WRS) [*Ross and Eaton*, 1997; *Welford and Clowes*, 2006]. Our model provides further support for this crustal anomaly and its significance, distribution and detailed characteristics will be explored through waveform modeling in section 4.5.

4.3. LVZ Revealed by the RFs and Inversion

Unlike the upper crustal HVZ, the existence of a thick midcrustal LVZ has not been reported nor widely accepted in the study region. To quantify this anomalous structure, we subdivide our RFs data set into three classes based on the strength of the negative phase preceding Pms. Figure 3a shows a representative RF from each class, among which RW5 exhibits the largest negative phase at ~2.2 s. The Moho conversion and reverberation (PpPms) arrive at ~4.3 s and ~15.0 s, respectively, after the *P* wave arrival. The RF from EDM shows a moderate-sized negative phase at ~3.2 s, followed by a Pms at ~4.9 s. In comparison, the RF from CLA shows significantly reduced energy at the expected times for both this negative arrival (at ~3.5 s) and Pms (at ~6.4 s).

High-frequency RFs exhibit similar trends to the low-frequency counterparts despite waveform complexities. The RFs from RW5 and EDM both contain broad negative phases preceding Pms. In the latter case, distinct arrivals at ~2 s (negative) and ~2.5 s (positive) are consistent with the corresponding phases in *Eaton and Cassidy* [1996]. These two arrivals could be attributed to the top and bottom reflections from a sharp midcrustal low-velocity layer. The modeling and interpretation of these phases are nonunique but vital for the estimation of characteristics (i.e., width, depth, and strength) of crustal LVZs. *P* wave conversions and reverberations at station CLA are exceptionally weak, which suggest relatively smooth, gradational velocity

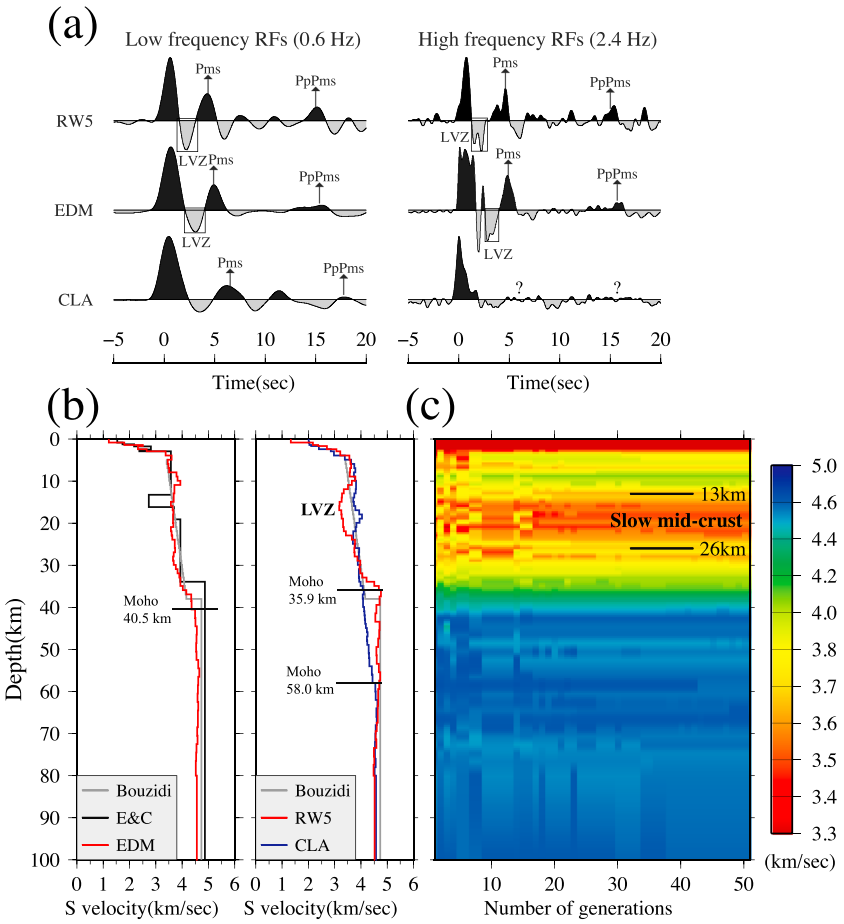

Figure 3. (a) Sample RFs showing the waveforms from stations residing on a LVZ (RW5), a relatively low-velocity middle crust (EDM) and a gradient crust (CLA), respectively. The Pms and PpPms phases are indicated by arrows. The phases that potentially indicate the existence of a low-velocity structure are enclosed by the rectangles. (b) Shear velocity models from this and previous studies. The definition of the model names are Bouzidi (scaled 1-D shear velocity model of *Bouzidi et al.* [2002]), EC96 (shear velocity model of *Eaton and Cassidy* [1996]), EDM (shear velocity model of station EDM from this study), RW5 (shear velocity model of station RW5 from this study), and CLA (shear velocity model of station CLA from this study). The Moho depths and the LVZ are labeled. (c) The color-coded velocity profile for the nonlinear inversion results from station EDM based on the genetic algorithm. The *y* and *x* axes denote the depth and the generation number, respectively. The horizontal lines delineate the depth ranges of the middle crust with shear velocity below the regional average.

variations in the underlying crust. This finding is consistent with the observation of a diffused Moho in *Lemieux et al.* [2000] for the same region.

The presence of a first-order crustal LVZ beneath central Alberta is substantiated through iterative inversions of the RFs. The optimal damping parameter, which links RF misfit with model smoothness, is chosen based on the turning point of the misfit-roughness norm curve [*Ammon et al.*, 1990]. The RFs from two frequency ranges are weighted equally. The misfit between the observed and simulated RFs decreases with the increasing number of iterations, and the inverse problem is terminated when the misfit curve is convergent. The best fit model for EDM (Figure 3b) shows a high-velocity layer at ~10 km depth with an approximate thickness of 3 km. Beneath this layer, the shear wave speed in the middle and lower crust is generally lower than the regional average [*Bouzidi et al.*, 2002]. At the base of the crust, the Moho is approximated by a velocity gradient, rather than a sharp interface, due to vertical averaging. Based on the midpoint of this steep velocity increase, we determine the Moho depth to be 40.5 ± 2 km beneath EDM, consistent with those estimated from P-Pms differential time (4.9 s in EDM) in the RFs and reflection seismic data (38–40 km) [*Bouzidi et al.*, 2002; *French et al.*, 2009]. Moho depths from all three studies are approximately 4 km larger than the proposed values by *Eaton and Cassidy* [1996] (from here, EC96).

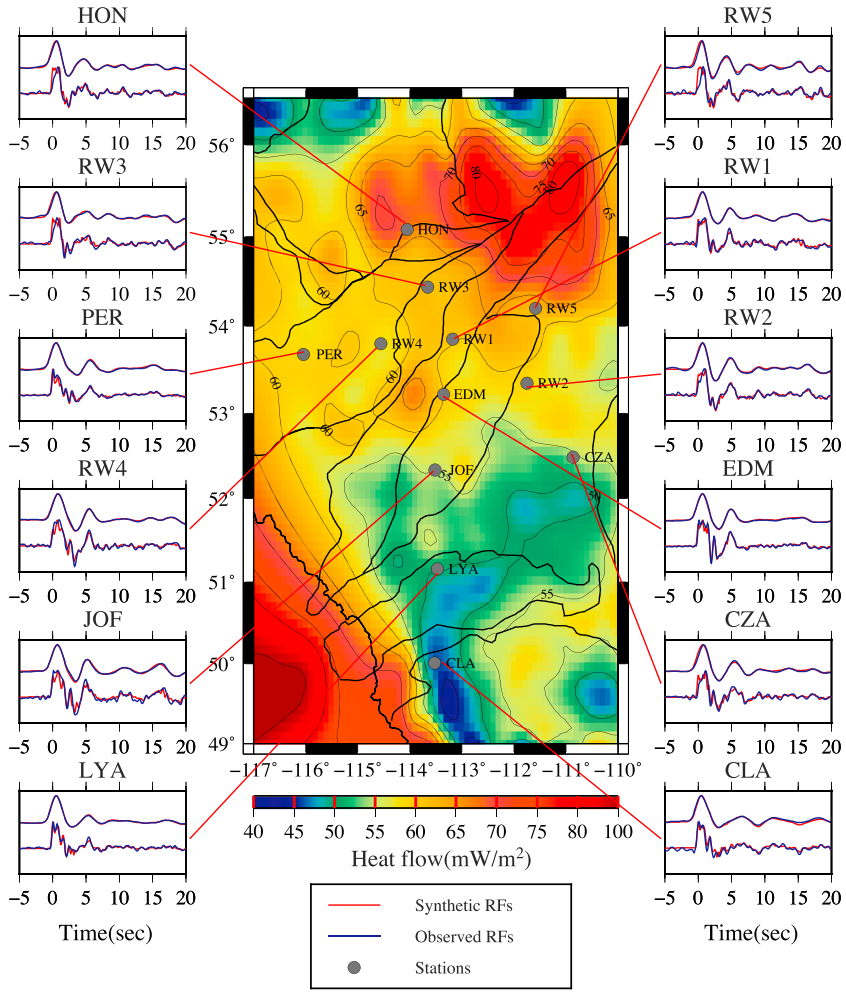

Figure 4. Waveform fitting results of all stations displayed on a regional heat flow map [*Majorowicz and Grasby*, 2010]. The synthetic and observed RFs are shown in red and blue colors, respectively. Stations with prominent LVZs are generally located within zones of enhanced heat flow.

The most significant difference between EC96 and our model of EDM (see Figure 3) is the structure in the middle and lower crust. In the former study, a thin LVZ was identified between 13 and 16 km with an average shear velocity of ~2.9 km/s. This is inconsistent with the middle crust in our model, which suggests an average shear velocity of ~3.5 km/s in depth range of ~12 to 25 km. The lower crust in EC96 is ~0.3 km/s faster than our model at comparable depths. These differences may be partially attributed to the difference in the waveforms of the stacked RFs. Our data benefited from a longer deployment time (1990–2011) of station EDM, while the EC96 model was limited to tens of recordings from the early 1990s. Differences in modeling strategy may also have contributed to the outcomes of these models. EC96 utilized a forward modeling approach, which emphasized the waveforms in the 1–2.5 s window at the expense of waveforms immediately proceeding Pms (see Figure 3 of EC96). Our study adopted an inverse approach based on an exhaustive search in the solution space for models that match a greater portion of the crustal RFs.

The ability to model the waveforms prior to Pms is essential for the understanding of the structure below the upper crust. In our study, the contrasting structures beneath stations RW5 and CLA highlight the two end-member models of the middle crust in Alberta. The crust beneath station RW5 (Figure 3b) contains a strong LVZ in the depth range of 12–25 km and a relatively sharp Moho at 36 km depth. The minimum shear velocity is 0.35 km/s slower than that beneath EDM. On the other hand, shear velocities comparable with the regional average increase monotonically with depth beneath CLA, as only a minor velocity reversal is visible at ~16 km depth, and the Moho is significantly weaker than that beneath the former region.

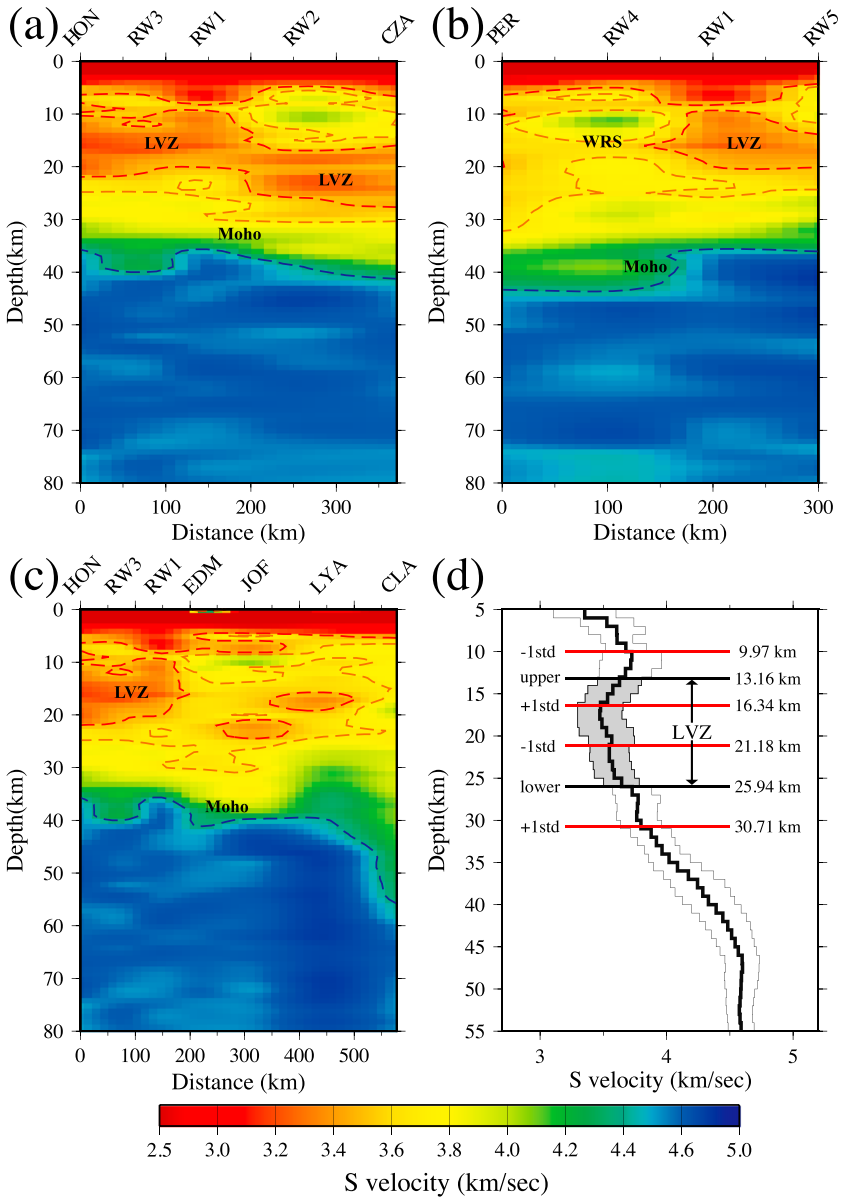

Figure 5. The crustal shear velocities beneath cross sections (a) A-A′, (b) B-B′ and (c) C-C′. The color-coded velocity profiles show shear velocities ranging from 2.5 to 3.7 km/s in the middle crust. The lower crustal velocities are represented by yellow to green colors ranging from 3.7 to 4.7 km/s. Upper mantle velocities in excess of 4.7 km/s are indicated by dark blue colors. The blue dashed lines mark the Moho depth based on a threshold $Vs = 4.6$ km/s. The red solid lines and orange dashed lines denote 3.5 km/s and 3.7 km/s contours, respectively. WRS = Winagami reflection sequence. (d) The average shear velocity model for the entire array. The shaded region shows the extent of the LVZ. The thick black lines mark the upper and lower boundaries of the LVZ within 1 standard deviation (denoted by the thick red lines). The thin black lines along the profile indicate 1 standard deviation of the average velocity at each depth.

Nonuniqueness is a well-documented pitfall of linear inversion of RFs. The solution of the inverse problem can be affected by the starting model [*Ammon et al.*, 1990] where an improper choice may steer the solution toward a local minimum. In addition to performing a series of inversions with perturbed starting models [*Ammon et al.*, 1990; *Mangino et al.*, 1993; *Wilde-Piórko and Grad*, 2002], we conduct a global solution search in model space based on the genetic algorithm (GA) [*Shibutani et al.*, 1996]. This method simulates gene evolution in biological systems and solves nonlinear inverse problems through complete global optimization [*Sambridge and Drijkoningen*, 1992]. The emergence (at the tenth generation) and stabilization of a broad middle crust with relatively low velocity (Figure 3c) are clearly demonstrated in the case of EDM.

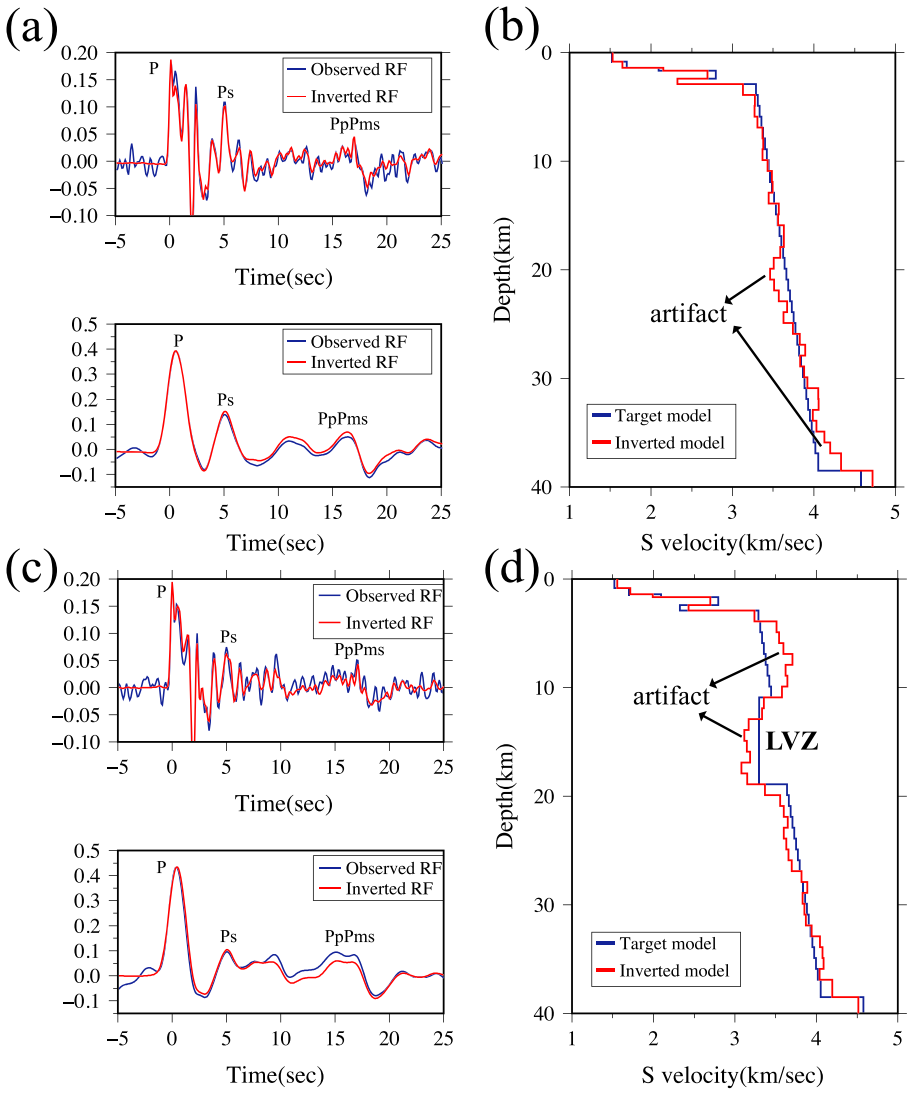

Figure 6. Results of waveform simulations that determine the inversion artifacts. (a) The waveform fitting results of the high- (top) and low- (bottom) frequency RFs. The blue and red lines represent the observed and inverted RFs, respectively. (b) A model showing a gradational crust (blue). The optimal model recovered from the inversion is shown in red color. (c) The waveform fitting results for the second synthetic test with an input low-velocity structure. (d) The recovered model (red) based on the input structure (blue).

Despite minor differences in the absolute velocities, the optimization-based model also requires a relatively slow middle crust to match the observed RFs. The consistency between two different inversion techniques increases our confidence in the results of the linear inversions.

The results of waveform inversions for all available stations in central Alberta are superimposed on the regional heat flow map of *Majorowicz and Grasby* [2010] (Figure 4). All stations exhibit satisfactory results where at least 90% of the energy of the observed *P*-to-*S* converted waveforms can be recovered using the final model. The depth and strength of the LVZ vary broadly in central Alberta (Figure 5). Along the southeast trending A-A′ profile (Figure 5a) from HON to CZA, the LVZ exhibits a southeast dipping morphology with a semi-uniform thickness of ~10 km based on the depth range between 3.5 km/s contour lines. The apparent LVZ depth difference between RW1 (13 km) and RW2 (23 km) marks an effective transition from shallow to deep LVZ initiation depths. Along the B-B′ profile (Figure 5b), the crust in the west (PER and RW4) is dominated by the HVZ. The LVZ increases its significance toward the east (RW1 and RW5). Finally, along

the north-south profile (Figure 5c), the midcrustal LVZ is the most pronounced beneath HON and gradually weakens toward central Alberta (near EDM and JOF) where the crustal velocities fall below the regional average. The crust beneath LYA contains a very thin (~5 km) layer with shear velocities less than 3.5 km/s. On average, the LVZ is best observed in the depth range of 13–26 km with an approximate minimum velocity of 3.4 km/s (Figure 5d).

4.4. Robustness of the HVZ and LVZ

On average, the HVZ from our RF analysis shows a thickness of 6 km and a velocity of ~3.7 km/s in southern WCSB. The presence of both HVZ and LVZ, which cause sizeable shear velocity gradients with opposite signs at 5–10 km and 10–16 km depths, inevitably raises questions about the depth resolution of the data and potential trade-offs in velocity. Hence, we perform waveform simulations to (1) quantify potential model biases and (2) provide further constraints on the characteristics of the HVZ and LVZ. In the first test, we generate synthetic RFs by using a simple gradient model with 1% Gaussian noise. The synthetic RFs are subsequently modeled following the same inversion procedures outlined in section 3. The recovered model (Figure 6b) preserves the gradational crust and shows only a ~0.2 km/s underestimation of the shear velocity at midcrustal depths, which is significantly less than the observed LVZ (~0.5 km/s) at RW5 and HON. The thickness of the artificial LVZ (~5 km) is also notably smaller than that beneath stations (e.g., EDM, ~20 km) with an average low-velocity middle crust.

In the second test, we introduce an 8 km thick LVZ into the middle crust. The presumed shear velocity (3.3 km/s) and spatial scale of the LVZ closely resemble those of the observed profiles beneath RW1, RW2, and RW5. The inversion successfully recovers the LVZ (Figure 6d), but the scale of the LVZ is exaggerated by ~0.11 km/s, and an anomalous HVZ is placed immediately above the LVZ. The average recovered *Vs* is ~0.24 km/s faster than the input linear velocity gradient. From these results, we conclude that (1) the gradational crust can be accurately resolved at middle and lower crustal depths, and (2) in the presence of the LVZ, the inverted model tends to exaggerate the scale of the LVZ and introduces an overlying high-velocity structure. Further experiments using an input high-velocity upper crust (see Figures S1 and S2 of supporting information) suggest minimal ($<$0.1 km/s) artifacts at midcrustal depths.

4.5. Waveform Modeling

A suite of synthetic waveforms is computed to assess the robustness of the models obtained from waveform inversions. Through a careful examination of waveform responses to model changes at various depths, we aim to provide further assessments on (1) the need for a midcrustal LVZ in central Alberta and (2) the potential trade-offs between LVZ and HVZ, especially for stations RW4 and PER. In the first experiment, we introduce a 6 km thick high-velocity layer with an average velocity of 3.9 km/s to the upper crust. We then gradually decrease the velocity of the middle crust from 3.66 km/s to 2.93 km/s, which effectively transforms the gradational middle crust into a LVZ (Figure 7a). The corresponding synthetic waveforms are compared with the RF from station HON, which is an average station with a mild HVZ and a significant midcrustal LVZ according to the waveform inversions. To simplify the solutions, our calculations ignore the effects of sediments, which mainly affect the RFs in the first 2 s and often cause the *P* wave signal to shift from zero time [*Sheehan et al.*, 1995] (see Figure 7b). A model with only a HVZ successfully recovers the first negative phase (labeled 1 in Figure 7b), which originates from the bottom of the HVZ from model 1.0 (Figure 7a), but fails to explain the presence of phase 2 (negative) in Figure 7b. After introducing a LVZ, the synthetic waveforms significantly improve the quality of phase 2 where the amplitude is proportional to the strength of the LVZ. However, the sharp velocity increases at the base of the LVZ cause conversions with abnormally high amplitudes (phase 3), which are inconsistent with the waveforms of the observed RFs.

To improve the model fit, we replace the sharp lower interface of the LVZ by a gradient structure (Figure 7c). This modification reduces the impedance contrast between the LVZ and the underlying crust, hence effectively suppressing the positive conversion (phase 3) trailing the dual negative phases 1 and 2 in Figures 7b and 7d. To improve the waveform match between the simulated and observed RFs, a third experiment was introduced in which the LVZ is fixed at 2.96 km/s while its thicknesses vary from 10 to 18 km (Figure 7e). The purpose of increasing LVZ thickness is to reduce the velocity gradient leading to the LVZ. The resulting synthetic RFs (Figure 7f) not only successfully recover the two negative peaks but also minimize the positive conversions. Summarizing the results of all three experiments, we conclude

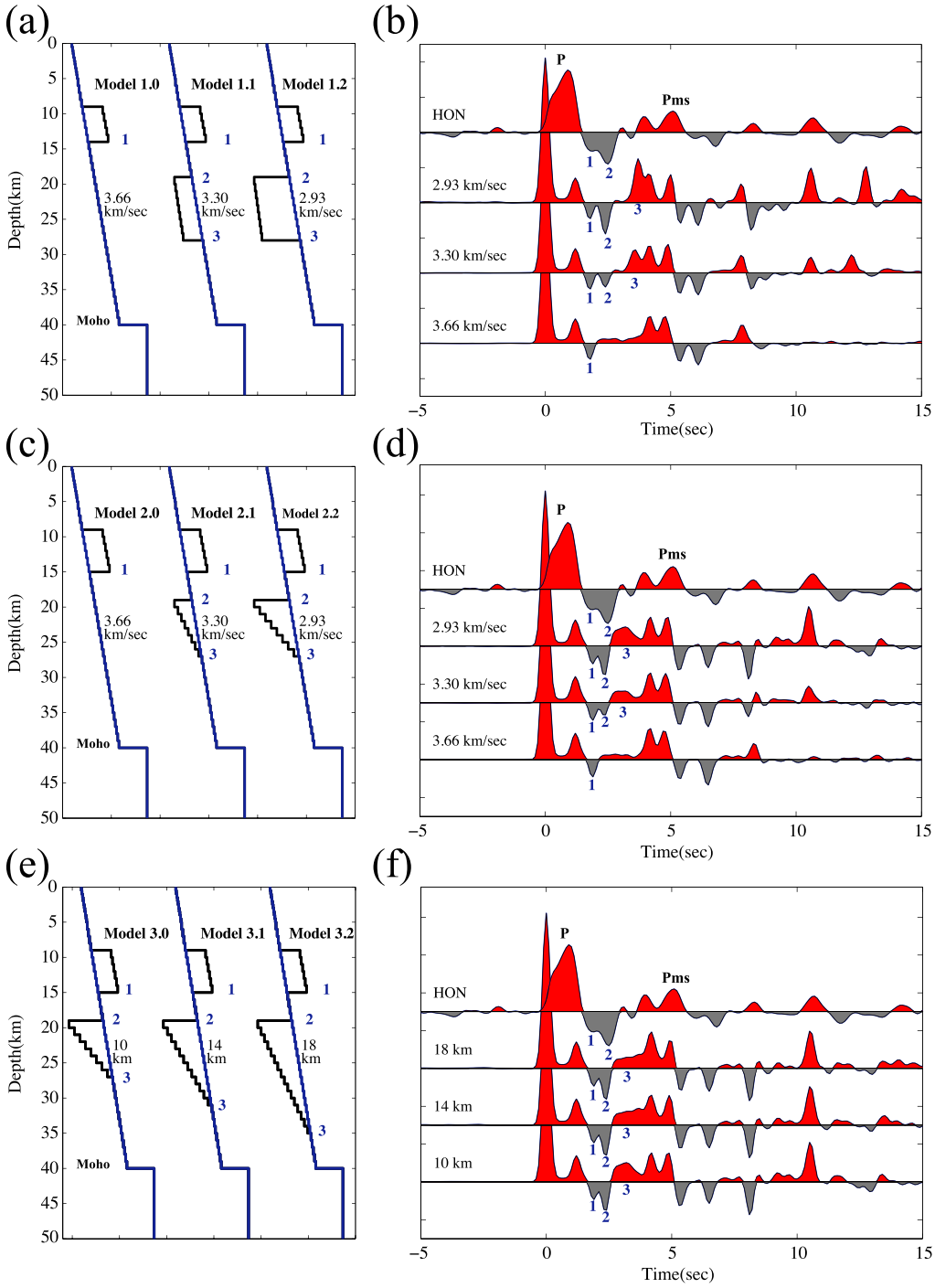

Figure 7. (a) Input models (black) that contain a HVZ at shallow crustal depth. The LVZs with velocities from high to low are inserted to the middle crust (model 1.0 to 1.2). The labeled values indicate the velocities at the top of the LVZ. The model shown in blue color represents the background velocity, and the numbers mark the locations of velocity jumps. (b) Simulated waveforms from the input models. The numbers indicate the phases generated by the interfaces in Figure 7a. The top trace is the waveform from station HON where a significant LVZ is revealed by our study. (c) Input models with a smaller velocity gradient at the bottom of the LVZ (model 2.0 to 2.2). (d) The synthetic waveforms computed based on models from Figure 7c. (e) Input models containing LVZs with various thicknesses (model 3.0 to 3.2). (f) Simulated waveforms from models shown in Figure 7e.

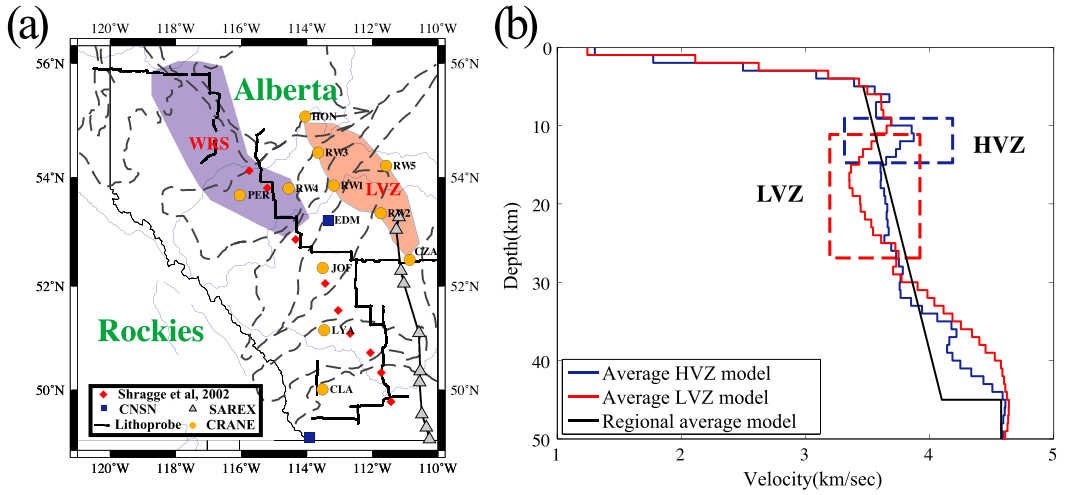

Figure 8. (a) A map showing the distribution of two model categories. The region underlain by strong LVZs is marked by red color. Stations showing a dominant HVZ spatially overlap with the WRS. The distribution of the WRS is shown in blue color. The symbols on the map indicate the location of earlier seismic surveys and the broadband stations used in this study. (b) The average shear velocity models for stations underlain by LVZs (red) and the WRS (blue). The regional average model (black) from *Bouzidi et al.* [2002] is also plotted for reference. The LVZ and HVZ structures are highlighted by the enclosed areas in red and blue colors, respectively.

that (1) a model with a HVZ above a broad (>14 km) LVZ is essential in matching the observed waveforms, (2) the scale of the LVZ should be larger than that of the HVZ to properly account for the amplitude difference between the negative peaks, and (3) the LVZ exhibits a reduced gradient toward its lower boundary, which prevents the model from generating an artificial positive phase before Pms.

4.6. Average Models in Various Tectonic Domains

The inverted seismic velocities from RFs vary significantly across the various tectonic regimes. The most prominent LVZs, as indicated by a shear velocity <3.5 km/s and a thickness value larger than 10 km (see Figure 5 for thicknesses and velocities), are mainly distributed along the STZ and Proterozoic magmatic arcs (e.g., HON, RW1, RW2, RW3, and CZA) (see Figure 1 for locations). The remaining stations in central Alberta (EDM and JOF) show a relatively mild but slow middle crust with shear velocities of ~3.6 km/s. Two southern stations, LYA and CLA, which are located on the Archean crust, show either a sharp low-velocity layer with shear velocity less than 3.5 km/s (the former) or a major crustal gradient (the latter).

The remaining stations, RW4 and PER, exhibit average midcrustal velocities under a prominent HVZ. The spatial distribution of those two stations provides additional insights into the nature of the HVZs. PER and RW4 reside on the Proterozoic accreted Wabamun domain (Figures 1 and 8), where WRS, a large-scale mafic magma intrusion, has been reported by the earlier seismic surveys [*Ross and Eaton*, 1997; *Welford and Clowes*, 2006]. The possible connection of the observed HVZs to WRS will be discussed in detail in section 5.1.

To explore the systematic spatial variation of velocity, we divide the stations into two groups according to the various crustal structures (HVZ versus LVZ) and calculate the average velocity for each group. Their spatial coverage is illustrated in Figure 8a with the distribution of WRS and LVZ obtained from *Welford and Clowes* [2006] and this study, respectively. The differences between the average models of WRS and LVZ can be clearly recognized in Figure 8b. The former model in the zone of WRS shows a prominent HVZ atop an otherwise gradational crust, while the latter model contains a thick (~12 km) LVZ with the lowest velocity of 3.36 km/s. The high-velocity lid structure overlying the LVZ can also be observed in the latter region, but its amplitude is visibly lower than that of the averaged WRS model (see Figure 8a, blue region).

The observed LVZs represent previously undisclosed large-scale midcrustal structures in central Alberta with an average thickness of ~12 km and a lateral dimension up to 200 km. The apparent model differences in various parts of the study region (see Figure 8b) reflect different tectonic environments and movements in the Proterozoic eon, and henceforth may be critical for understanding the tectonic history of western Laurentia.

5. Discussion

5.1. General Assessments

The broadband seismic data enable us to examine the crust beneath the southern WCSB, where distinctive low- and high-velocity structures are resolved by RF imaging. The most significant HVZ is observed beneath station RW4, where the underlying ~3 km thick high-velocity (~4 km/s) layer is incompatible with an otherwise gradational, ~3.55 km/s crust. This value is substantially larger than the expected level of modeling artifacts (~0.2 km/s) due to the trade-off between a HVZ and LVZ (see Figure 6). The magmatic history of the region surrounding RW4 offers a plausible explanation. RW4 resides in the Wabamun domain, a Proterozoic accreted terrane where a mafic sill complex (WRS) intrudes into the upper crust [*Ross and Eaton*, 1997; *Welford and Clowes*, 2006]. The composition of the upper crust is likely altered by the intrusion of numerous subhorizontal sills with doleritic composition, which increases the bulk velocity [*Welford and Clowes*, 2006] and forms a high-velocity (~3.8 km/s) structure. It has been suggested that the Winagami reflector resides in the depth range of 6.5 and 16.5 km [*Ross and Eaton*, 1997], which is in reasonable agreement with our estimates (8–14 km; see Figure 8). Post-collisional magmatism during the convergence of the Slave and Rae provinces, which provides a probable source for melt intrusion [*Ross and Eaton*, 1997], are likely responsible for the HVZ observed in the western part of our study region.

The most important finding, hence the main focus, of this study is the prominent midcrustal LVZ in eastern-central Alberta. From the existing literature, crustal LVZs have been reported in several tectonically active or Cretaceous orogens, such as the Tibetan Plateau [*Kind et al.*, 1996], Alps [*Mueller and Landisman*, 1966], Andes [*Schmitz et al.*, 1997], and Apennines [*Ökeler et al.*, 2009], where they are characterized by lateral dimensions of hundreds of kilometers. In contrast, cratons consisting of old and stable continental crusts [*Grotzinger and Jordan*, 2010] are nearly unaffected by tectonothermal events since the Precambrian and generally exhibit minimal geophysical or geological signature of a thick, definitive LVZ. An exception is the North China craton, where a LVZ has been documented as two westward dipping layers and interpreted as the remnant of subducted upper to middle continental crust beneath the Ordos Basin [*Zheng et al.*, 2009]. In comparison with the crustal structure beneath the North China craton, the LVZ in central Alberta is distinctively thicker (by 10+ km) and wider (by ~200 km), more resembling the scales of the LVZs beneath tectonically active regions. Despite the apparent age difference between young orogens and the Precambrian central Alberta, the presence of crustal LVZs with comparable scales in both tectonic provinces offers important clues about the possible links in their genesis. The remainder of this section will review and differentiate between four candidate mechanisms for the generation of crustal LVZs beneath the Precambrian basement of Alberta, which include (1) partial melting of the crust [*Kind et al.*, 1996; *Nelson et al.*, 1996], (2) serpentinite coupled with a subduction process [*Eaton and Cassidy*, 1996; *Li et al.,* 2003b], (3) anisotropy [*Zorin et al.*, 2002], and (4) the intrusion of crystallized granitic bodies [*Masson et al.*, 1998; *Bogdanova et al.*, 2006].

5.2. Partial Melting

In the first scenario, partial melting in the crust has been revealed by multidisciplinary studies of the Tibetan Plateau, where the ongoing collision between the Indian and Eurasian plates triggers massive magmatic activities that are manifested in both surface geology and crustal structure. The LVZ covers most of the Tibetan middle crust at the depths between 20 and 40 km [*Yang et al.*, 2012]. Its existence has been attributed to crustal thickening [*Nelson et al.*, 1996] and the presence of aqueous fluids or high H_2O contents [*Rapine et al.*, 2003; *Caldwell et al.*, 2009], all of which could effectively lower the melting temperature, initiate partial melting process, and significantly decrease seismic wave velocities [*Sato et al.*, 1989]. In theory, the presence of partial melt would offer a simple explanation for a crustal LVZ, including the observed anomaly beneath eastern-central Alberta. However, regional electromagnetic surveys [*Boerner et al.*, 2000] and seismic reflection explorations [*Ross et al.*, 1995; *Lemieux et al.*, 2000; *Bouzidi et al.*, 2002] have discovered no evidence for a partial melting zone. Major tectonic events, e.g., continent-continent collision and post-collisional magmatism [*Ross et al.*, 1991, 1995, 2000], have long ceased since the assembly of western Canadian Shield in the Proterozoic eon. Without significant reactivation of the basement crust in the Phanerozoic eon [*Ross and Eaton*, 1999], residual melt and its thermal imprints are unlikely to survive over one billion years of lithosphere cooling in western Laurentia [*Ross*, 2002].

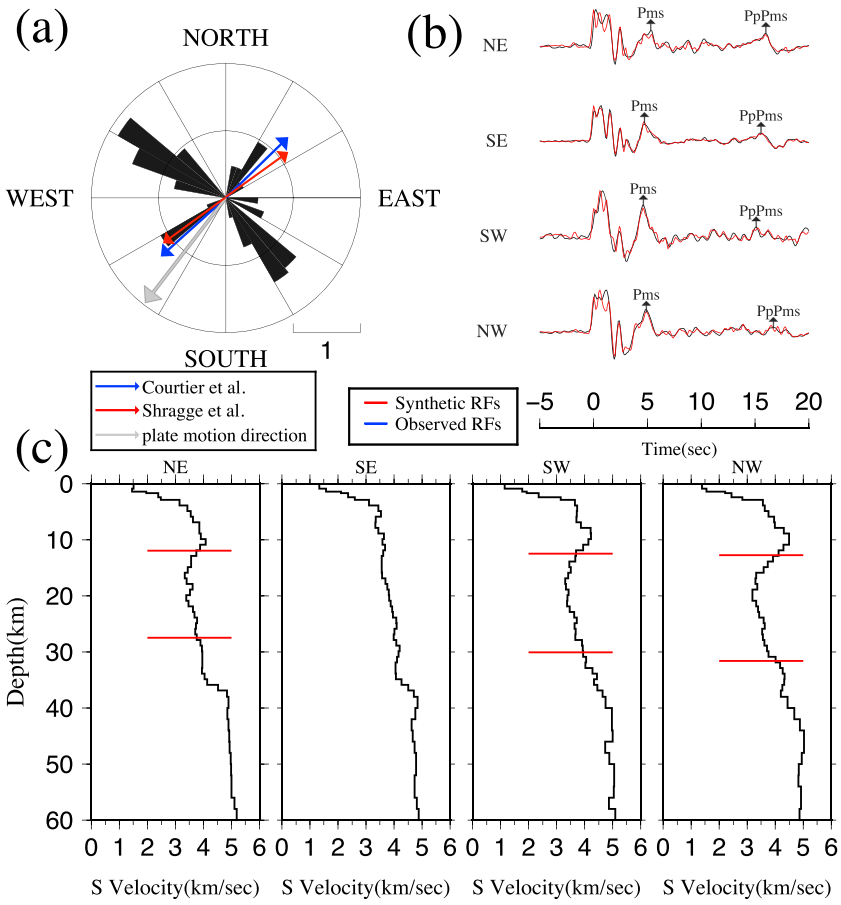

Figure 9. (a) A rose diagram showing the back azimuths of data recorded by station EDM on a logarithmic scale. The red and blue arrows show the shear wave splitting measurements of *Shragge et al.* [2002] and *Courtier et al.* [2010], respectively, beneath station EDM. The grey arrow indicates the plate motion direction. (b) The observed (blue) and simulated (red) RFs for four back azimuth quadrants for station EDM. (c) Inverted models from the four quadrants are shown in Figure 9b. Three out of four azimuth ranges show a relatively low-velocity middle crust; the lone exception is along the southeastern direction, which suggests a gradational crust. The red lines mark the boundaries of the low-velocity middle crust.

5.3. Serpentinization Associated With Subduction

An alternative explanation is the presence of serpentinites, which can originate either from subducted oceanic crust containing subducted abyssal serpentinites or serpentinized layer formed at the subduction plane interface [*Deschamps et al.*, 2013]. *Eaton and Cassidy* [1996] interpreted a thin, 3 km thick LVZ in central Alberta as a serpentinized peridotite layer associated with obducted oceanic plate due to its comparable shear velocity (2.9 ± 0.2 km/s) with that of serpentinite (2.79 ± 0.44 km/s) at 15 km depth. In comparison with this earlier model, the observed middle crust in our study is 0.6 km/s faster. Aside from the velocity mismatch, the spatial scale of the LVZ in the east part of the study region (~10 km × 200 km) is considerably larger than that expected for a localized serpentinite layer [*Eaton and Cassidy*, 1996]. Perhaps more importantly, serpentinite breaks down at temperatures above 600–700°C [*Deschamps et al.*, 2013], while geochemical evidence from Chipman mafic dikes reveals temperatures in excess of 750°C along the STZ [*Flowers et al.*, 2006]. In other words, serpentinite is unlikely to remain stable during craton evolution since its original formation from Paleoproterozoic subduction.

5.4. Anisotropy

Anisotropy has also been cited as a possible mechanism of LVZs [*Zorin et al.*, 2002] since the reorientation of minerals under regional stress field could reduce the seismic velocity along certain orientations. Earlier studies of seismic anisotropy have suggested dominant (fast) orientations of 33–43° in the mantle (Figure 9a)

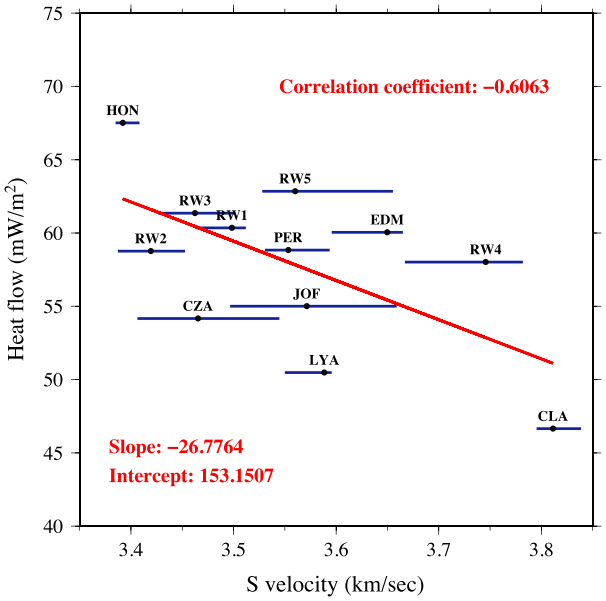

Figure 10. The correlation between heat flow and average shear velocity. The red line shows the computed linear regression, and the blue line at each data point indicates the range of average shear velocities for the inverted models from the first 20 iterations.

[*Shragge et al.*, 2002; *Courtier et al.*, 2010] beneath Alberta. These values are in rough alignment with the present-day plate motion (see Figure 9a). While our source-receiver paths are mainly oriented in the northwest-southeast direction, which coincides with the expected slow shear wave direction, the consistent waveforms (Figure 9b) and inverted models (Figure 9c) based on stacked RFs from four quadrants show little, if any, directional dependence of the crustal velocities. Similar results are obtained for other stations in the region of study. In other words, anisotropy is unlikely to play a major role in the presence of the observed midcrustal LVZ.

5.5. Granite Intrusion

Based on evidence from regional heat flow, observed seismic velocities and tectonic history, we propose that a regional-scale granitic body formed under a compressional tectonic setting is the most probable explanation for the observed LVZs. The heat flow in central and southern Alberta (see Figure 4) is, to first order, spatially correlated with the LVZ distribution. Regions underlain by a strong LVZ generally reside in high heat flow ($>60\,mW/m^2$) regions associated with accreted terranes and magmatic arcs, whereas stations without distinctive LVZ signatures (LYA and CLA) are both confined to an anomalously low heat flow ($<50\,mW/m^2$) zone in the Archean southern Alberta. This trend is consistent with earlier reports of increased heat flow from Archean craton(s) to the surrounding younger Precambrian terrains [*Ballard and Pollack*, 1987; *Rudnick and Fountain*, 1995]. Variable radiogenic heat generation in different tectonic provinces likely contributes to the observed heat flow variation in Alberta [*Bachu*, 1993]. For instance, it has long been suggested that the spatial variation of heat flow, as manifested by regional thermal anomalies, could reflect variable degrees of granite intrusion into the basement [*Bachu*, 1988]. This hypothesis is supported by the abundant granite-granitoids discovered in drill core samples along the Rimbey magmatic arc [*Ross et al.*, 1991]. A crustal model containing a granite-rich layer provides an attractive explanation both for the observed heat flow variation and for the LVZ in eastern-central Alberta. A statistical analysis indicates an overall correlation of 0.60 between heat flow and average crustal velocity (Figure 10). Since the heat flow map is constructed based on the interpolation of measurements at sparse locations in Alberta, a potential error of 25% [*Majorowicz*, 1996] could possibly weaken the connection between the LVZ and heat flow. Still, the moderately correlated crustal velocities and heat flow values could imply a common contributing factor involving granite.

The hypothesis of granite intrusion is supported by the average shear velocity (3.45 ± 0.30 km/s) of the observed midcrustal LVZ. Based on the average reported compressional velocities of crustal rocks [e.g., *Christensen and Mooney*, 1995], we obtain average shear velocities of granite-granodiorite of 3.599 km/s and 3.593 km/s at 15 and 20 km depths, respectively, assuming an average Poisson's ratio of 0.25 and average temperatures of 225°C and 309°C. These values are well within the uncertainties of average velocity of the observed LVZ (see Figure 5d) in this study, a robust measurement only marginally affected by the nonuniqueness of the inversions. In other words, a model containing a granitic midcrustal LVZ is favored by the observed seismic velocities in western Laurentia. A granitic LVZ has been reported in various tectonic frameworks. An upper crustal LVZ caused by a granite intrusion is discovered in the Variscan orogenic zone of southwest Ireland [*Masson et al.*, 1998]. Similar findings in the East European Craton [*Bogdanova et al.*, 2006], which consists of Mesoproterozoic granitic rocks formed by the remelting of the upper crust, could also represent a contemporaneous analogue.

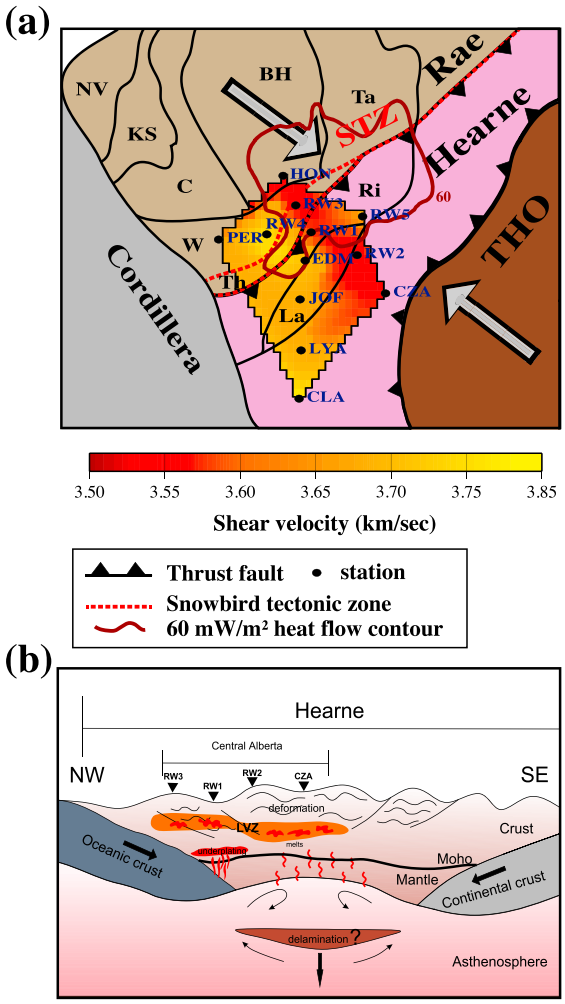

Figure 11. (a) A schematic regional tectonic map showing a possible tectonic framework for the generation of a crustal LVZ. The average shear velocities for all stations are displayed using a color map. The 60 mW/m^2 heat flow contour highlights the overlap between high heat flow regions and areas of below average shear velocities. (b) A schematic diagram to demonstrate the major tectonic events including the subduction of oceanic crust, collisional crustal thickening, and lithosphere delamination; all three mechanisms could contribute to the presence of crustal LVZ in Alberta. The vertical scale of the crust has been exaggerated for a better visual inspection.

5.6. Tectonic Implications

The most robust observation is the LVZ beneath eastern-central Alberta stations, where below average shear velocities at shallow and middle crustal depths were reported by recent findings from noise-correlation tomography [*Gu and Shen*, 2015]. The entrapment of the Hearne province [*Ross et al.*, 2000], which comprises the basement of the southern WCSB during the Paleoproterozoic eon, provides a rich tectonic environment for the formation of a granite-rich crustal layer. It has been long documented that the Hearne province was once bounded by the coeval subduction of oceanic lithosphere along the STZ and continental lithosphere in the Trans-Hudson orogen [*Ross et al.*, 1995, 2000]. The STZ is a NE trending gravity and magnetic anomaly [*Flowers et al.*, 2006], splitting the western Churchill province into the Hearne and Rae domains. The role of the STZ during the assembly of Churchill province remains debated, as it has been interpreted both as an intercontinental suture [*Hoffman*, 1988; *Ross et al.*, 2000; *Berman et al.*, 2007] and as an intracontinental fault/shear zone [*Lewry et al.*, 1981; *Hanmer et al.*, 1995]. In the former (and more accepted) hypothesis, the intercontinental origin favors a collisional event between the Hearne and Rae provinces [*Berman et al.*, 2007] approximately 1.9 billion years ago. Central Alberta covers the southern extension of the STZ, where the Thorsby domain was formed as a marginal basin in the Proterozoic eon and eventually subducted beneath the Hearne province due to basin closure [*Ross et al.*, 2000]. During the proposed subduction, the descending oceanic crust underwent dehydration and triggered partial melting within the mantle wedge. Magma would propagate upward and underplate the lower crust, as is evident in the Cree Lake Zone [*Annesley et al.*, 2005] and southern Alberta [*Clowes et al.*, 2002]. Magma underplating could contribute to mid-crustal melting, which produces leucogranite discovered in Rimbey magmatic belt [*Ross et al.*, 1991]. To the east of the Hearne province, the THO collided with Hearne ~1.80 Ga and initiated extensive NW-SE crustal shortening, thickening and deformation. The syn-collisonal or post-collisional tectonothermal activities associated with crustal shortening significantly increased the radiogenic heat production in the crust, which could elevate the temperature sufficiently to cause the anatexis process at mid-to-upper crustal depths [*Chen and Grapes*, 2007] and induce granitic intrusions. Lithosphere delamination due to shortened and gravitationally unstable mantle lithosphere [*Ross et al.*, 2000] may enhance crustal melting further. In the event of lithosphere delamination [*Ross et al.*, 2000], increased mantle heat flux could also facilitate partial melting near the base of the crust and increase the volume of granite within the crust.

Orogeny with ongoing subduction and extensive LVZ in the central Andes presents a modern analogy for the Paleoproterozoic events in eastern-central Alberta. A regional midcrustal low-velocity layer has been

observed beneath broad areas in the central Andes, which was interpreted as the brittle/ductile transition between upper and lower crust in the presence of partial melt [*Beck and Zandt*, 2002]. The crust beneath the mountain belt exhibits lower than average velocities and a felsic granite composition [*Zandt et al.*, 1994; *Beck and Zandt*, 2002]. The similarity between the tectonic settings of the Hearne province and the Andes, despite the apparent age difference, favors a common model of tectonic evolution with episodes of subduction, crustal shortening and elevation, as well as a possible delamination of the mantle root.

In summary, the presence of granitic body in the middle crust beneath central Alberta is favored by (1) heat flow and crustal shear velocity correlation, (2) comparable average velocity of the LVZ with that of granite in the middle crust, and (3) an ideal dual-subduction tectonic setting (Figure 11a) for the generation of regional-scale partial melting. The schematic diagram (Figure 11b) summarizes the tectonic processes leading to the formation of the LVZ. The middle crust underwent partial melting due to (1) magma and underplating initiated by the subduction of the oceanic plates, (2) increased heat generation due to the thickened crust, and (3) protracted heating after the delamination of the mantle root. The region of partial melt could be further enlarged by the intrusion of melt into the country rock, or even through the process of decompression melting in response to lithosphere exhumation. During the millions of years of lithosphere cooling since the Precambrian, the molten crust would crystallize to solid rocks and eventually form a granite-rich midcrustal LVZ.

In short, our study provides new evidence for an upper crustal HVZ and a midcrustal LVZ in central Alberta. The boundary and connection between these two features remain unclear. In view of their nonoverlapping geographical distributions (see Figure 8a) and strengths (see Figure 8b), distinct episodes of Proterozoic magmatism are more likely to be the explanation instead of a common origin.

6. Conclusions

Orogens are the attestations of the most striking collisional events in the Earth's tectonic history. The resultant crustal deformation, which is generally recognizable from magnificent mountain ranges (e.g., Himalayan mountain belt), can cause partial melting and the formation of intrusive bodies with a granitic composition. Over 1.7 billion years ago, Himalayan-scale orogenesis and crustal deformation most likely transpired near the THO, a Precambrian orogen with residual imprints of crustal magmatism in the form of a LVZ in spite of erosion and subsequent tectonic events. The detailed composition of the observed crustal LVZ remains speculative, though its existence and scale (200 km wide and 10 km thick) beneath the southern WCSB are strongly supported by heat flow observations, elastic properties of granite, and inversions of RFs computed from thousands of teleseismic events in this study. The presence of LVZ will undoubtedly lend new insights on the early assembly and evolution of western Laurentia.

Acknowledgments
We thank Tom Chacko, Larry M Heaman, and Martyn Unsworth for their insightful suggestions for improvements. We thank Jacek Majorowicz for kindly sending us the regional heat flow data. We also thank the host families of CRANE seismic stations for their long-term support of our work. This study is supported by National Science and Engineering Council (NSERC) and Alberta Energy Regulator (AER). Seismic data are publicly available from IRIS data management center. Figures in the paper are plotted by using Generic Mapping Tools [*Wessel et al.*, 2013].

References

Abers, G. A. (2005), Seismic low-velocity layer at the top of subducting slabs: Observations, predictions, and systematics, *Phys. Earth Planet. Inter.*, *149*(1), 7–29.

Ammon, C. J., G. E. Randall, and G. Zandt (1990), On the nonuniqueness of receiver function inversions, *J. Geophys. Res.*, *95*(B10), 15,303–15,318, doi:10.1029/JB095iB10p15303.

Annesley, I. R., C. Madore, and P. Portella (2005), Geology and thermotectonic evolution of the western margin of the Trans-Hudson Orogen: Evidence from the eastern sub-Athabasca basement, Saskatchewan, *Can. J. Earth Sci.*, *42*(4), 573–597.

Bachu, S. (1988), Analysis of heat transfer processes and geothermal pattern in the Alberta Basin, Canada, *J. Geophys. Res.*, *93*(B7), 7767–7781, doi:10.1029/JB093iB07p07767.

Bachu, S. (1993), Basement heat flow in the Western Canada sedimentary basin, *Tectonophysics*, *222*(1), 119–133.

Ballard, S., and H. N. Pollack (1987), Diversion of heat by Archean cratons: A model for southern Africa, *Earth Planet. Sci. Lett.*, *85*(1), 253–264.

Beck, S. L., and G. Zandt (2002), The nature of orogenic crust in the central Andes, *J. Geophys. Res.*, *107*(B10), 2230, doi:10.1029/2000JB000124.

Berman, R., W. Davis, and S. Pehrsson (2007), Collisional Snowbird tectonic zone resurrected: Growth of Laurentia during the 1.9 Ga accretionary phase of the Hudsonian orogeny, *Geology*, *35*(10), 911–914.

Boerner, D., R. Kurtz, J. Craven, G. Ross, and F. Jones (2000), A synthesis of electromagnetic studies in the Lithoprobe Alberta Basement Transect: Constraints on Paleoproterozoic indentation tectonics, *Can. J. Earth Sci.*, *37*(11), 1509–1534.

Bogdanova, S., R. Gorbatschev, M. Grad, T. Janik, A. Guterch, E. Kozlovskaya, G. Motuza, G. Skridlaite, V. Starostenko, and L. Taran (2006), EUROBRIDGE: New insight into the geodynamic evolution of the East European Craton, *Geol. Soc. London Mem.*, *32*(1), 599–625.

Bouzidi, Y., D. R. Schmitt, R. A. Burwash, and E. R. Kanasewich (2002), Depth migration of deep seismic reflection profiles: Crustal thickness variations in Alberta, *Can. J. Earth Sci.*, *39*(3), 331–350.

Burdick, L. J., and C. A. Langston (1977), Modeling crustal structure through the use of converted phases in teleseismic body-wave forms, *Bull. Seismol. Soc. Am.*, *67*(3), 677–691.

Caldwell, W. B., S. L. Klemperer, S. S. Rai, and J. F. Lawrence (2009), Partial melt in the upper-middle crust of the northwest Himalaya revealed by Rayleigh wave dispersion, *Tectonophysics*, *477*(1), 58–65.

Cassidy, J. F. (1992), Numerical experiments in broadband receiver function analysis, *Bull. Seismol. Soc. Am.*, *82*(3), 1453–1474.
Chen, G. N., and R. H. Grapes (2007), *Granite Genesis: In-situ Melting and Crustal Evolution*, pp. 1–278, Springer, Dordrecht, Netherlands.
Chen, Y., and F. Niu (2013), Ray-parameter based stacking and enhanced pre-conditioning for stable inversion of receiver function data, *Geophys. J. Int.*, doi:10.1093/gji/ggt179.
Chmielowski, J., G. Zandt, and C. Haberland (1999), The Central Andean Altiplano-Puna magma body, *Geophys. Res. Lett.*, *26*(6), 783–786, doi:10.1029/1999GL900078.
Christensen, N. I., and W. D. Mooney (1995), Seismic velocity structure and composition of the continental crust: A global view, *J. Geophys. Res.*, *100*(B6), 9761–9788, doi:10.1029/95JB00259.
Clayton, R. W., and R. A. Wiggins (1976), Source shape estimation and deconvolution of teleseismic bodywaves, *Geophys. J. R. Astron. Soc.*, *47*(1), 151–177.
Clowes, R. M., A. J. Calvert, D. W. Eaton, Z. Hajnal, J. Hall, and G. M. Ross (1996), LITHOPROBE reflection studies of Archean and Proterozoic crust in Canada, *Tectonophysics*, *264*(1), 65–88.
Clowes, R. M., M. J. Burianyk, A. R. Gorman, and E. R. Kanasewich (2002), Crustal velocity structure from SAREX, the southern Alberta refraction experiment, *Can. J. Earth Sci.*, *39*(3), 351–373.
Contenti, S. M., Y. J. Gu, and L. Shen (2012), An integrated crustal analysis of craton-terrane transition, paper presented at AGU Fall Meeting Abstracts.
Corrigan, D., S. Pehrsson, N. Wodicka, and E. De Kemp (2009), The Palaeoproterozoic Trans-Hudson Orogen: A prototype of modern accretionary processes, *Geol. Soc. London Spec. Publ.*, *327*(1), 457–479.
Courtier, A. M., J. B. Gaherty, J. Revenaugh, M. G. Bostock, and E. J. Garnero (2010), Seismic anisotropy associated with continental lithosphere accretion beneath the CANOE array, northwestern Canada, *Geology*, *38*(10), 887–890.
Crotwell, H. P., and T. J. Owens (2005), Automated receiver function processing, *Seismol. Res. Lett.*, *76*(6), 702–709.
Deschamps, F., M. Godard, S. E. Guillot, and K. Hattori (2013), Geochemistry of subduction zone serpentinites: A review, *Lithos*, *178*, 96–127.
Eaton, D. W., and J. F. Cassidy (1996), A relic Proterozoic subduction zone in western Canada: New evidence from seismic reflection and receiver function data, *Geophys. Res. Lett.*, *23*(25), 3791–3794, doi:10.1029/96GL03619.
Eaton, D. W., G. M. Ross, and R. M. Clowes (1999), Seismic-reflection and potential-field studies of the Vulcan structure, western Canada: A Paleoproterozoic pyrenees?, *J. Geophys. Res.*, *104*(B10), 23,255–23,269, doi:10.1029/1999JB900204.
Flowers, R., S. Bowring, and M. Williams (2006), Timescales and significance of high-pressure, high-temperature metamorphism and mafic dike anatexis, Snowbird tectonic zone, Canada, *Contrib. Mineral. Petrol.*, *151*(5), 558–581.
French, S., K. Fischer, E. Syracuse, and M. Wysession (2009), Crustal structure beneath the Florida-to-Edmonton broadband seismometer array, *Geophys. Res. Lett.*, *36*, L08309, doi:10.1029/2008GL036331.
Grotzinger, J., and T. H. Jordan (2010), *Understanding Earth*, 6th ed., W. H. Freeman and Company, New York.
Gu, Y. J. (2010), *Arrays and Array Methods in Global Seismology*, Springer, Berlin.
Gu, Y. J., and L. Shen (2012), Microseismic noise from large ice-covered lakes?, *Bull. Seismol. Soc. Am.*, *102*(3), 1155–1166.
Gu, Y. J., and L. Shen (2015), Noise correlation tomography of Southwest Western Canada Sedimentary Basin, *Geophys. J. Int.*, *202*(1), 142–162, doi:10.1093/gji/ggv100.
Gu, Y. J., A. Ökeler, S. Contenti, K. Kocon, L. Shen, and K. Brzak (2009), Broadband seismic array deployment and data analysis in Alberta, *CSEG Recorder, September*, 37–44.
Gu, Y. J., A. Ökeler, L. Shen, and S. Contenti (2011), the Canadian rockies and Alberta network (crane): New constraints on the rockies and western Canada sedimentary basin, *Seismol. Res. Lett.*, *82*(4), 575–588.
Gu, Y. J., Y. Zhang, M. D. Sacchi, Y. Chen, and S. Contenti (2015), Sharp mantle transition from cratons to Cordillera in southwestern Canada, *J. Geophys. Res. Solid Earth*, *120*, 5051–5069, doi:10.1002/2014JB011802.
Hanmer, S., M. Williams, and C. Kopf (1995), Striding-Athabasca mylonite zone: Implications for the Archean and Early Proterozoic tectonics of the western Canadian Shield, *Can. J. Earth Sci.*, *32*(2), 178–196.
Hoffman, P. F. (1988), United Plates of America, the birth of a craton-Early Proterozoic assembly and growth of Laurentia, *Annu. Rev. Earth Planet. Sci.*, *16*, 543–603.
James, D. E., F. Niu, and J. Rokosky (2003), Crustal structure of the Kaapvaal craton and its significance for early crustal evolution, *Lithos*, *71*(2), 413–429.
Kanasewich, E., R. Clowes, and C. McCloughan (1969), A buried Precambrian rift in western Canada, *Tectonophysics*, *8*(4), 513–527.
Kennett, B., E. Engdahl, and R. Buland (1995), Constraints on seismic velocities in the Earth from traveltimes, *Geophys. J. Int.*, *122*(1), 108–124.
Kind, R., G. Kosarev, and N. Petersen (1995), Receiver functions at the stations of the German Regional Seismic Network (GRSN), *Geophys. J. Int.*, *121*(1), 191–202.
Kind, R., J. Ni, W. Zhao, J. Wu, X. Yuan, L. Zhao, E. Sandvol, C. Reese, J. Nabelek, and T. Hearn (1996), Evidence from earthquake data for a partially molten crustal layer in southern Tibet, *Science*, *274*(5293), 1692–1694.
Kumar, M. R., D. Ramesh, J. Saul, D. Sarkar, and R. Kind (2002), Crustal structure and upper mantle stratigraphy of the Arabian shield, *Geophys. Res. Lett.*, *29*(8), 130–131, doi:10.1029/2001GL014530.
Laske, G., G. Masters, Z. Ma, and M. Pasyanos (2013), Update on CRUST1. 0-A 1-degree global model of Earth's crust, paper presented at Geophys. Res. Abstracts.
Lemieux, S., G. M. Ross, and F. A. Cook (2000), Crustal geometry and tectonic evolution of the Archean crystalline basement beneath the southern Alberta Plains, from new seismic reflection and potential-field studies, *Can. J. Earth Sci.*, *37*(11), 1473–1491.
Lewry, J., M. Stauffer, and S. Fumerton (1981), A cordilleran-type batholitic belt in the Churchill province in northern Saskatchewan, *Precambrian Res.*, *14*(3), 277–313.
Li, H., W. Su, C.-Y. Wang, Z. Huang, and Z. Lv (2010), Ambient noise Love wave tomography in the eastern margin of the Tibetan plateau, *Tectonophysics*, *491*(1), 194–204.
Li, S., M. J. Unsworth, J. R. Booker, W. Wei, H. Tan, and A. G. Jones (2003a), Partial melt or aqueous fluid in the mid-crust of Southern Tibet? Constraints from INDEPTH magnetotelluric data, *Geophys. J. Int.*, *153*(2), 289–304.
Li, X., G. Bock, A. Vafidis, R. Kind, H.-P. Harjes, W. Hanka, K. Wylegalla, M. Van Der Meijde, and X. Yuan (2003b), Receiver function study of the Hellenic subduction zone: Imaging crustal thickness variations and the oceanic Moho of the descending African lithosphere, *Geophys. J. Int.*, *155*(2), 733–748.
Lucas, S., A. Green, Z. Hajnal, D. White, J. Lewry, K. Ashton, W. Weber, and R. Clowes (1993), Deep seismic profile across a Proterozoic collision zone: Surprises at depth, *Nature*, *363*, 339–342.
Majorowicz, J., and S. E. Grasby (2010), Heat flow, depth-temperature variations and stored thermal energy for enhanced geothermal systems in Canada, *J. Geophys. Eng.*, *7*(3), 232–241.

Majorowicz, J. A. (1996), Anomalous heat flow regime in the western margin of the North American craton, Canada, *J. Geodyn.*, *21*(2), 123–140.
Mangino, S. G., G. Zandt, and C. J. Ammon (1993), The receiver structure beneath Mina, Nevada, *Bull. Seismol. Soc. Am.*, *83*(2), 542–560.
Masson, F., A. Jacob, C. Prodehl, P. Readman, P. Shannon, A. Schulze, and U. Enderle (1998), A wide-angle seismic traverse through the Variscan of southwest Ireland, *Geophys. J. Int.*, *134*(3), 689–705.
Monsalve, H., J. F. Pacheco, C. A. Vargas, and Y. A. Morales (2013), Crustal velocity structure beneath the western Andes of Colombian using receiver-function inversion, *J. South Am. Earth Sci.*, *48*, 106–122.
Mueller, S. (1977), A new model of the continental crust, *Geophys. Monogr. Ser.*, *20*, 289–317.
Mueller, S., and M. Landisman (1966), Seismic studies of the Earth's crust in continents I: Evidence for a low-velocity zone in the upper part of the lithosphere*, *Geophys. J. R. Astron. Soc.*, *10*(5), 525–538.
Nelson, K. D., et al. (1996), Partially molten middle crust beneath southern Tibet: Synthesis of project INDEPTH results, *Science*, *274*(5293), 1684–1688.
Ökeler, A., Y. J. Gu, A. Lerner-Lam, and M. S. Steckler (2009), Seismic structure of the southern Apennines as revealed by waveform modelling of regional surface waves, *Geophys. J. Int.*, *178*(3), 1473–1492.
Owens, T. J., G. Zandt, and S. R. Taylor (1984), Seismic evidence for an ancient rift beneath the Cumberland Plateau, Tennessee: A detailed analysis of broadband teleseismic P waveforms, *J. Geophys. Res.*, *89*(B9), 7783–7795, doi:10.1029/JB089iB09p07783.
Petford, N., A. Cruden, K. McCaffrey, and J.-L. Vigneresse (2000), Granite magma formation, transport and emplacement in the Earth's crust, *Nature*, *408*(6813), 669–673.
Rapine, R., F. Tilmann, M. West, J. Ni, and A. Rodgers (2003), Crustal structure of northern and southern Tibet from surface wave dispersion analysis, *J. Geophys. Res.*, *108*(B2), 2120, doi:10.1029/2001JB000445.
Ross, G. M. (2002), Evolution of Precambrian continental lithosphere in Western Canada: Results from lithoprobe studies in Alberta and beyond, *Can. J. Earth Sci.*, *39*(3), 413–437.
Ross, G. M., and D. W. Eaton (1997), Winagami reflection sequence: Seismic evidence for postcollisional magmatism in the Proterozoic of western Canada, *Geology*, *25*(3), 199–202.
Ross, G. M., and D. W. Eaton (1999), Basement reactivation in the Alberta Basin: Observational constraints and mechanical rationale, *Bull. Can. Pet. Geol.*, *47*(4), 391–411.
Ross, G. M., R. R. Parrish, M. E. Villeneuve, and S. A. Bowring (1991), Geophysics and geochronology of the crystalline basement of the Alberta Basin, western Canada, *Can. J. Earth Sci.*, *28*(4), 512–522.
Ross, G. M., B. Milkereit, D. Eaton, D. White, E. R. Kanasewich, and M. J. A. Burianyk (1995), Paleoproterozoic collisional orogen beneath the western Canada sedimentary basin imaged by lithoprobe crustal seismic-reflection data, *Geology*, *23*(3), 195–199.
Ross, G. M., D. W. Eaton, D. E. Boerner, and W. Miles (2000), Tectonic entrapment and its role in the evolution of continental lithosphere: An example from the Precambrian of western Canada, *Tectonics*, *19*(1), 116–134, doi:10.1029/1999TC900047.
Rudnick, R. L., and D. M. Fountain (1995), Nature and composition of the continental crust: A lower crustal perspective, *Rev. Geophys.*, *33*(3), 267–309, doi:10.1029/95RG01302.
Sambridge, M., and G. Drijkoningen (1992), Genetic algorithms in seismic waveform inversion, *Geophys. J. Int.*, *109*(2), 323–342.
Sato, H., I. S. Sacks, and T. Murase (1989), The use of laboratory velocity data for estimating temperature and partial melt fraction in the low-velocity zone: Comparison with heat flow and electrical conductivity studies, *J. Geophys. Res.*, *94*(B5), 5689–5704, doi:10.1029/JB094iB05p05689.
Schmitz, M., W.-D. Heinsohn, and F. Schilling (1997), Seismic, gravity and petrological evidence for partial melt beneath the thickened central Andean crust (21–23 S), *Tectonophysics*, *270*(3), 313–326.
Schultz, R., V. Stern, and Y. J. Gu (2014), An investigation of seismicity clustered near the Cordel Field, west central Alberta, and its relation to a nearby disposal well, *J. Geophys. Res. Solid Earth*, *119*, 3410–3423, doi:10.1002/2013JB010836.
Sheehan, A. F., G. A. Abers, C. H. Jones, and A. L. Lerner-Lam (1995), Crustal thickness variations across the Colorado Rocky Mountains from teleseismic receiver functions, *J. Geophys. Res.*, *100*(B10), 20,391–20,404, doi:10.1029/95JB01966.
Shibutani, T., M. Sambridge, and B. Kennett (1996), Genetic algorithm inversion for receiver functions with application to crust and uppermost mantle structure beneath eastern Australia, *Geophys. Res. Lett.*, *23*(14), 1829–1832, doi:10.1029/96GL01671.
Shragge, J., M. Bostock, C. Bank, and R. Ellis (2002), Integrated teleseismic studies of the southern Alberta upper mantle, *Can. J. Earth Sci.*, *39*(3), 399–411.
Stern, T. A., D. Okaya, S. Kleffmann, M. Scherwath, S. Henrys, and F. J. Davey (2007), Geophysical exploration and dynamics of the Alpine Fault Zone, in *A Continental Plate Boundary: Tectonics at South Island, New Zealand*, *AGU Geophys. Monogr. Ser.*, vol. 175, edited by D. Okaya, T. Stern, and F. Davey, pp. 207–233, AGU, Washington, D. C.
Stern, V., R. Schultz, L. Shen, Y. Gu, and D. Eaton (2013), Alberta earthquake catalogue 2006–2010 (GIS data, point features), *Alberta Energy Regulator, Digital Data*, *17*.
St-Onge, M. R., M. P. Searle, and N. Wodicka (2006), Trans-Hudson orogen of North America and Himalaya-Karakoram-Tibetan orogen of Asia: Structural and thermal characteristics of the lower and upper plates, *Tectonics*, *25*, TC4006, doi:10.1029/2005TC001907.
Unsworth, M., et al. (2005), Crustal rheology of the Himalaya and Southern Tibet inferred from magnetotelluric data, *Nature*, *438*(7064), 78–81.
Ward, K. M., R. C. Porter, G. Zandt, S. L. Beck, L. S. Wagner, E. Minaya, and H. Tavera (2013), Ambient noise tomography across the Central Andes, *Geophys. J. Int.*, *194*(3), 1559–1573.
Wei, W., et al. (2001), Detection of widespread fluids in the Tibetan crust by magnetotelluric studies, *Science*, *292*(5517), 716–719.
Welford, J. K., and R. M. Clowes (2006), Three-dimensional seismic reflection investigation of the upper crustal Winagami sill complex of northwestern Alberta, Canada, *Geophys. J. Int.*, *166*(1), 155–169.
Wessel, P., W. H. Smith, R. Scharroo, J. Luis, and F. Wobbe (2013), Generic mapping tools: Improved version released, *Eos Trans. AGU*, *94*(45), 409–410, doi:10.1002/2013EO450001.
Wilde-Piórko, M., and M. Grad (2002), Crustal structure variation from the Precambrian to Palaeozoic platforms in Europe imaged by the inversion of teleseismic receiver functions—Project TOR, *Geophys. J. Int.*, *150*(1), 261–270.
Yang, Y., M. H. Ritzwoller, Y. Zheng, W. Shen, A. L. Levshin, and Z. Xie (2012), A synoptic view of the distribution and connectivity of the mid-crustal low velocity zone beneath Tibet, *J. Geophys. Res.*, *117*, B04303, doi:10.1029/2011JB008810.
Yuan, X., J. Ni, R. Kind, J. Mechie, and E. Sandvol (1997), Lithospheric and upper mantle structure of southern Tibet from a seismological passive source experiment, *J. Geophys. Res.*, *102*(B12), 27,491–27,500, doi:10.1029/97JB02379.
Yuan, X., et al. (2000), Subduction and collision processes in the Central Andes constrained by converted seismic phases, *Nature*, *408*(6815), 958–961.

Zandt, G., A. A. Velasco, and S. L. Beck (1994), Composition and thickness of the southern Altiplano crust, Bolivia, *Geology*, *22*(11), 1003–1006.
Zelt, C. A., and R. Ellis (1989), Seismic structure of the crust and upper mantle in the Peace River Arch region, Canada, *J. Geophys. Res.*, *94*(B5), 5729–5744, doi:10.1029/JB094iB05p05729.
Zheng, T., L. Zhao, and R. Zhu (2009), New evidence from seismic imaging for subduction during assembly of the North China Craton, *Geology*, *37*(5), 395–398.
Zorin, Y. A., V. Mordvinova, E. K. Turutanov, B. Belichenko, A. Artemyev, G. Kosarev, and S. Gao (2002), Low seismic velocity layers in the Earth's crust beneath Eastern Siberia (Russia) and Central Mongolia: Receiver function data and their possible geological implication, *Tectonophysics*, *359*(3), 307–327.